COMPDYN 2011
III ECCOMAS Thematic Conference on
Computational Methods in Structural Dynamics and Earthquake Engineering
M. Papadrakakis, M. Fragiadakis, V. Plevris (eds.)
Corfu, Greece, 25–28 May 2011

CUTOFF WAVE NUMBERS FOR ENERGY-ORTHOGONAL TWENTY-NODE HEXAHEDRAL ELEMENTS

Francisco José Brito Castro

Departamento de Física Fundamental y Experimental, Universidad de La Laguna
Calle Mendez Nuñez 67- 2C, Santa Cruz de Tenerife 38001, SPAIN
fjbrito@ull.es

Key words: wave propagation, modal analysis, energy-orthogonal stiffness.

Abstract. *This paper studies the propagation of plane harmonic waves in unbounded media discretized by the standard twenty-node hexahedral finite element. The element stiffness matrix is split into basic and higher order components which are obtained from mean and deviatoric strain fields, respectively. This decomposition is applied to the elastic energy. Based on the properties of the higher order energy, two values of the wave number are selected. Depending on the desired precision one of those values can be used as optimum cutoff wave number to properly capture a wave field.*

1 INTRODUCTION

The wave propagation in solids is a so broad scientific subject that analytical solutions to the governing equation of motion exist for just the simplest cases and only approximate solutions are feasible for the others. One method for obtaining approximate solutions is to use numerical procedures, such as the finite element method, which often introduce phenomena that are not present in the physical system [1]. In references [2, 3] the wave propagation in solids is analyzed through.

The governing equation of motion for a homogeneous isotropic elastic solid may be summarized as

$$(\lambda + \mu)\nabla\nabla \cdot \mathbf{u} + \mu\nabla^2\mathbf{u} + \rho\mathbf{f} = \rho\ddot{\mathbf{u}} \tag{1}$$

where: the elastic constants for the material are λ and μ, the Lamé constants; ρ, the mass density per unit volume of the material; **u**, the displacement vector; **f**, the body force per unit mass of material.

The Lamé constants can be expressed as

$$\lambda = \frac{E\nu}{(1+\nu)(1-2\nu)}, \quad \mu = \frac{E}{2(1+\nu)} \tag{2}$$

where: E, Young´s modulus; ν, Poisson´s ratio for the material.

Let us consider the Helmholtz decomposition of the displacement vector as the gradient of a scalar and the curl of a zero divergence vector,

$$\mathbf{u} = \nabla\Phi + \nabla \times \mathbf{H}, \quad \nabla \cdot \mathbf{H} = 0 \tag{3}$$

The scalar potential Φ is associated with the dilatational part of the disturbance, and the vector potential **H** with the rotational part.

By considering Eq. (3), the governing equation of motion Eq. (1) is decomposed as two simplified wave equations, in the absence of body forces,

$$\nabla^2\Phi = \frac{1}{c_L^2}\frac{\partial^2\Phi}{\partial t^2}, \quad \nabla^2\mathbf{H} = \frac{1}{c_T^2}\frac{\partial^2\mathbf{H}}{\partial t^2} \tag{4}$$

where:

$$c_L = \left(\frac{\lambda + 2\mu}{\rho}\right)^{1/2}, \quad c_T = \left(\frac{\mu}{\rho}\right)^{1/2} \tag{5}$$

Bulk wave propagation refers to wave propagation in unbounded media; guided waves are those that require a boundary for their existence, such as surface waves, Lamb waves, and interface waves. This paper will focus on bulk wave propagation in unbounded media. By considering Eq. (4) we deduce that the dilatational and rotational bulk waves propagate without interaction in unbounded media with the velocities c_L and c_T, respectively. These two types of waves are coupled only on the boundary of the elastic solid, an obvious consequence of satisfying the boundary conditions. The dilatational and rotational bulk waves are also called primary (P) and secondary (S) waves, respectively.

In this paper we consider the propagation of uniform plane harmonic waves,

$$\mathbf{u} = A\hat{\mathbf{a}}\exp\left[i\left(\kappa\mathbf{n} \cdot \mathbf{r} - \omega t\right)\right] \tag{6}$$

where: A, amplitude of the wave; ω, radial frequency; κ, wave number; $\hat{\mathbf{a}}$, polarization vector, unit vector indicating the direction of the particle displacement; **n**, wave normal, unit vector indicating the direction of the wave propagation; **r**, position vector.

The wave number and the radial frequency will be

$$\kappa = \frac{2\pi}{\lambda} = \frac{\omega}{c}, \quad \omega = \frac{2\pi}{T} = 2\pi f \tag{7}$$

where: λ, wavelength; c, phase speed of the continuum; T, period of wave; f, cyclic frequency.

The longitudinal plane waves, where the displacements are in the direction of the wave normal and only normal stresses are acting along the wave front, are dilatational waves; nevertheless, the transverse plane waves, where the displacements are perpendicular to the wave normal and only shearing stresses are acting along the wave front, are rotational waves.

For isotropic elastic material, the relationship between strains and stresses, in the absence of initial strains and stresses, can be expressed in matrix form as

$$\begin{Bmatrix} \sigma_x & \sigma_y & \sigma_z & \tau_{xy} & \tau_{xz} & \tau_{yz} \end{Bmatrix}^t = \mathbf{E} \begin{Bmatrix} \varepsilon_x & \varepsilon_y & \varepsilon_z & \gamma_{xy} & \gamma_{xz} & \gamma_{yz} \end{Bmatrix}^t \tag{8}$$

where **E** is the elasticity matrix,

$$\mathbf{E} = \begin{bmatrix} \lambda+2\mu & \lambda & \lambda & 0 & 0 & 0 \\ \lambda & \lambda+2\mu & \lambda & 0 & 0 & 0 \\ \lambda & \lambda & \lambda+2\mu & 0 & 0 & 0 \\ 0 & 0 & 0 & \mu & 0 & 0 \\ 0 & 0 & 0 & 0 & \mu & 0 \\ 0 & 0 & 0 & 0 & 0 & \mu \end{bmatrix} \tag{9}$$

By considering Eq. (5), the elasticity matrix also can be expressed in the forms

$$\mathbf{E}_L = \rho c_L^2 \begin{bmatrix} 1 & p & p & 0 & 0 & 0 \\ p & 1 & p & 0 & 0 & 0 \\ p & p & 1 & 0 & 0 & 0 \\ 0 & 0 & 0 & q & 0 & 0 \\ 0 & 0 & 0 & 0 & q & 0 \\ 0 & 0 & 0 & 0 & 0 & q \end{bmatrix}, \quad \mathbf{E}_T = \rho c_T^2 \begin{bmatrix} \varepsilon & r & r & 0 & 0 & 0 \\ r & \varepsilon & r & 0 & 0 & 0 \\ r & r & \varepsilon & 0 & 0 & 0 \\ 0 & 0 & 0 & 1 & 0 & 0 \\ 0 & 0 & 0 & 0 & 1 & 0 \\ 0 & 0 & 0 & 0 & 0 & 1 \end{bmatrix} \tag{10}$$

where: $p = 1 - 2/\varepsilon$, $q = 1/\varepsilon$, $r = \varepsilon - 2$ and $\varepsilon = c_L^2 / c_T^2 = (\lambda + 2\mu)/\mu = (2 - 2\nu)/(1 - 2\nu)$. Since $0 \le \nu \le 1/2$ always, we deduce the inequality $c_L > c_T$.

The forms of the elasticity matrix given by the Eq. (10) will be useful to analyze the propagation of longitudinal and transverse waves, respectively.

This work essentially extends the author´s previous work on the eight-node quadrilateral and the six-node triangle [4, 5]. The elastic media is discretized by the standard twenty-node hexahedral finite element [6] with consistent mass matrix [7]. By splitting the strain-nodal displacements matrix into mean and deviatoric components

$$\mathbf{e}^e = \mathbf{B}^e \mathbf{x}^e = (\overline{\mathbf{B}}^e + \mathbf{B}_d^e)\mathbf{x}^e \tag{11}$$

$$\overline{\mathbf{B}}^e V^e = \int_V \mathbf{B}^e dV, \quad \mathbf{B}_d^e = \mathbf{B}^e - \overline{\mathbf{B}}^e \tag{12}$$

the element stiffness matrix will be

$$\mathbf{K}^e = \mathbf{K}_b^e + \mathbf{K}_h^e \tag{13}$$

$$\mathbf{K}_b^e = \int_V (\overline{\mathbf{B}}^e)^t \mathbf{E} \overline{\mathbf{B}}^e dV \tag{14}$$

$$\mathbf{K}_h^e = \int_V (\mathbf{B}_d^e)^t \mathbf{E} \mathbf{B}_d^e dV \tag{15}$$

where: $\mathbf{K}_b^e$, basic stiffness matrix; and $\mathbf{K}_h^e$, higher order stiffness matrix.

In this case the element stiffness matrix is decomposed in energy-orthogonal form [8]. The basic and higher order matrices are related to the mean and deviatoric strain fields,

$$\overline{\mathbf{e}}^e = \overline{\mathbf{B}}^e \mathbf{x}^e, \quad \mathbf{e}_d^e = \mathbf{B}_d^e \mathbf{x}^e \tag{16}$$

respectively.

The concept of energy-orthogonal stiffness matrix used in this paper was explicitly introduced by Bergan and Nygärd in the context of the Free Formulation [9], and by Felippa within the framework of the Parametrized Variational Principles [10].

The decomposition Eq. (13) holds for the complete model whenever $\mathbf{K}_b^e$ and $\mathbf{K}_h^e$ are independently assembled,

$$\mathbf{K} = \mathbf{K}_b + \mathbf{K}_h \tag{17}$$

This decomposition is also applied to the elastic energy of the finite element assemblage,

$$U = U_b + U_h \tag{18}$$

$$U_b = \tfrac{1}{2} \mathbf{x}^t \mathbf{F}_b, \quad \mathbf{F}_b = \mathbf{K}_b \mathbf{x} \tag{19}$$

$$U_h = \tfrac{1}{2} \mathbf{x}^t \mathbf{F}_h, \quad \mathbf{F}_h = \mathbf{K}_h \mathbf{x} \tag{20}$$

where: U_b, basic elastic energy; U_h, higher order elastic energy; $\mathbf{F}_b$ and $\mathbf{F}_h$, basic and higher order forces vector, respectively.

In this paper the dispersion properties and the elastic energy of both longitudinal and transverse waves are computed for the unbounded media discretized by regular meshes. If the exact solution of the problem consists of a constant stress state, the higher order elastic energy vanishes over each element. Similarly, as the solution converges on account of mesh refinement, the element energy is increasingly dominated by the basic energy. This behavior has been numerically verified for the standard twenty-node hexahedral finite element in the context of modal analysis [11].

The above heuristic argument shows that the higher order elastic energy may be regarded as a local error indicator [10]. Although this assumption is based largely on numerical experiments motivates to explore the relationship between the higher order elastic energy and the numerical dispersion introduced by the finite element method.

In this paper the behavior of the higher order elastic energy is investigated and based on its properties two values of the wave number are selected as reference values. The use of one of those values as optimum cutoff wave number to properly capture a wave field is investigated. The concept is extended to define an optimum cutoff frequency to properly capture the natural modes of a solid.

The distinctive contributions of this paper over the author´s previous works [4, 5] are related to the consideration of hexahedral elements both moderately and highly distorted. These ones could be useful for the 3D modelling of structural elements.

2 WAVES IN UNBOUNDED MEDIA

2.1 Characteristic equations

In a solid discretized by the finite element method the equations of equilibrium governing its linear dynamic response may be cast in matrix form

$$\mathbf{M}\ddot{\mathbf{x}} + \mathbf{C}\dot{\mathbf{x}} + \mathbf{K}\mathbf{x} = \mathbf{f} \tag{21}$$

where **M**, **C** and **K** are the mass, damping, and stiffness matrices; **f** is the external load vector; and **x** is the displacement vector of the finite element assemblage [12].

The homogeneous and isotropic unbounded media is discretized by a regular mesh of standard twenty-node hexahedral elements, Figure 1. The nodal lattice has four nodes per unit cell which are labeled *A*, *B, C* and *D*, respectively. The node *A* is a corner one, whereas the nodes *B, C* and *D* are mid-side ones. Specifically, the elements analyzed are of brick geometry. Different meshes with the same element volume can be obtained by changing the aspect ratio parameter, γ; where, $1 \geq \gamma > 0$. The finite element analysis will be performed by using the rectangular coordinate system Σ: XYZ.

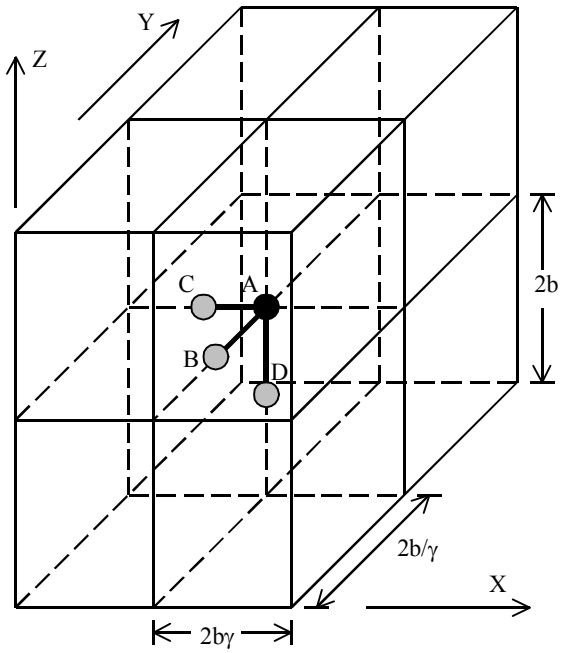

Figure 1: Regular mesh of standard twenty-node hexahedral elements and unit cell.

The characteristic equations can be found assuming uniform plane harmonic waves with different amplitudes in each node of the unit cell,

$$\mathbf{u} = A_i \hat{\mathbf{a}} \cos\left[\kappa \mathbf{n} \cdot \mathbf{r} - \omega t\right], \quad i = 1,2,3,4 \tag{22}$$

where: A_1, A_2, A_3 and A_4, wave amplitudes in the nodes *A*, *C, B* and *D*, respectively.

The wave normal **n** and the assumed polarization vector $\hat{\mathbf{a}}$ are related to the rectangular coordinate system Σp, obtained from Σ by three successive rotations defined by the Euler angles, Figure 2. For longitudinal waves, $\mathbf{n} = \hat{\mathbf{a}} = \mathbf{i}_p$; for transverse waves, $\hat{\mathbf{a}} = \mathbf{j}_p$ or $\hat{\mathbf{a}} = \mathbf{k}_p$.

The components of the displacement vector **u** with respect to the coordinate system Σ are obtained from the ones respect to the coordinate system Σp by

$$\{u \quad v \quad w\}^t = \mathbf{R}^t \{u_p \quad v_p \quad w_p\}^t \tag{23}$$

The transformation matrix will be

$$\mathbf{R} = \mathbf{CBA} \tag{24}$$

where

$$\mathbf{A} = \begin{bmatrix} \cos\phi & \sin\phi & 0 \\ -\sin\phi & \cos\phi & 0 \\ 0 & 0 & 1 \end{bmatrix}, \quad \mathbf{B} = \begin{bmatrix} 1 & 0 & 0 \\ 0 & \cos\theta & \sin\theta \\ 0 & -\sin\theta & \cos\theta \end{bmatrix}, \quad \mathbf{C} = \begin{bmatrix} \cos\psi & \sin\psi & 0 \\ -\sin\psi & \cos\psi & 0 \\ 0 & 0 & 1 \end{bmatrix} \tag{25}$$

are the transformation matrices for the rotations Σ → Σa, Σa → Σb and Σb → Σp, respectively. The three Euler angles are called the precession ϕ, the nutation θ, and the spin ψ [13].

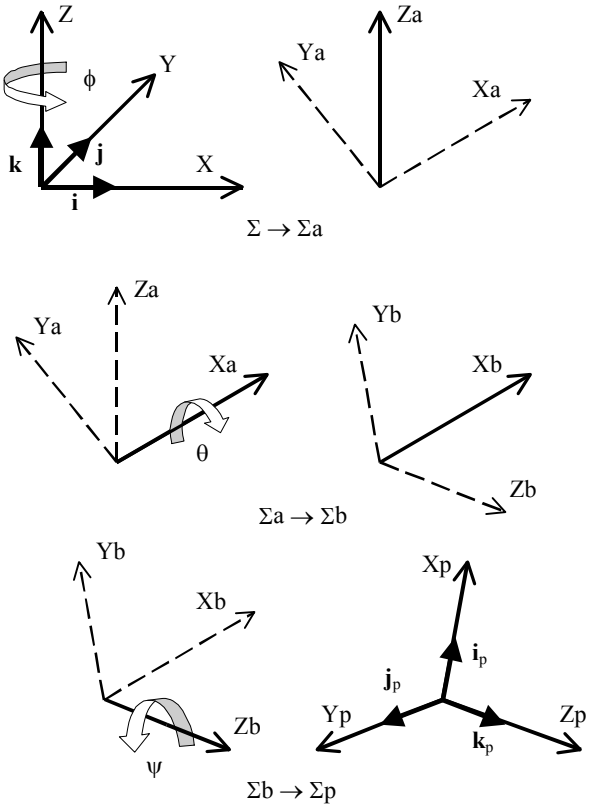

Figure 2: Rectangular coordinate transformation corresponding to three successive rotations defined by the Euler angles.

By considering the homogeneous part of Eq. (21) with damping neglected and substituting the assumed harmonic solutions we obtain the characteristic equation for each node of the unit cell by the equilibrium of nodal forces into the direction of the particle displacement [14].

The four characteristic equations form a system of homogeneous algebraic equations,

$$\mathbf{ZA} = \begin{bmatrix} z_{11} & z_{12} & z_{13} & z_{14} \\ z_{21} & z_{22} & z_{23} & z_{24} \\ z_{31} & z_{32} & z_{33} & z_{34} \\ z_{41} & z_{42} & z_{43} & z_{44} \end{bmatrix} \begin{Bmatrix} A_1 \\ A_2 \\ A_3 \\ A_4 \end{Bmatrix} = \begin{Bmatrix} 0 \\ 0 \\ 0 \\ 0 \end{Bmatrix} \tag{26}$$

$$z_{ij} = a_{ij}(m,\phi,\theta,\psi,\nu,\gamma) + \varpi^2 b_{ij}(m,\phi,\theta,\psi,\nu,\gamma) \tag{27}$$

$$m = \frac{b\kappa}{\pi} = \frac{2b}{\lambda}, \quad \varpi = \frac{2b}{c}\omega \tag{28}$$

where: m, dimensionless wave number; b, half of the cubic element size; ϖ, dimensionless frequency of the discretized media.

The dimensionless wave number will be $m_L = b\kappa_L/\pi$ and $m_T = b\kappa_T/\pi$ for longitudinal and transverse waves, respectively. From the continuum frequencies and Eq. (7) we obtain the relationship $m_T/m_L = c_L/c_T$. From $c_L > c_T$ we deduce the inequality $m_L < m_T$.

2.2 Dispersion equations

The system of homogeneous algebraic equations given in Eq. (26) has a non-trivial solution only if the matrix **Z** is singular; that is,

$$\det\left[\mathbf{Z}(m,\phi,\theta,\psi,\nu,\gamma,\varpi)\right] = 0 \tag{29}$$

By considering Eq. (27), from Eq. (29) we obtain the quartic equation

$$q^4 + d_3 q^3 + d_2 q^2 + d_1 q + d_0 = 0 \tag{30}$$

where: $q = \varpi^2$; $d_i(m,\phi,\theta,\psi,\nu,\gamma)$, coefficients obtained from a_{ij} and b_{ij}.

Either of Eq. (29) and (30) is called a characteristic frequency equation for plane wave propagation.

It is an important fact that the n zeroes of a polynomial of degree $n \geq 1$ with complex coefficients depend continuously upon the coefficients [15]. Thus, sufficiently small changes in the coefficients of a polynomial can lead only to small changes in any zero. However there is no simple way to define a function which takes the n coefficients (all but the leading 1) of a monic polynomial of degree n to the n zeroes of the polynomial, since there is no natural way to define an ordering among the n zeroes. In the case of the quartic polynomial Eq. (30), this problem has been solved by obtaining the zeroes in closed form. Then, the components

$$q_i = q_i(d_0, d_1, d_2, d_3), \quad i = 1,2,3,4 \tag{31}$$

or, alternatively,

$$\varpi_i = \varpi_i(m,\phi,\theta,\psi,\nu,\gamma), \quad i = 1,2,3,4 \tag{32}$$

will be continuous functions precisely defined. They are called dispersion equations. Obviously, we suppose that the coefficients $d_i(m,\phi,\theta,\psi,\nu,\gamma)$ are also continuous functions.

Substituting Eq. (32) into Eq. (26), the wave amplitudes for each dispersion equation are produced. In this work, each set of linear algebraic equations is numerically solved by using the singular value decomposition method SVD [16].

The range of dimensionless wave number values where each dispersion equation represents the propagation of acoustic waves in the discretized media will be called the

acoustical branch of the dispersion equation. In order to determine the acoustical branches, a preliminary constraint condition over the dimension of the null space of **Z** must be imposed,

$$\dim\left[\mathbf{N}(\mathbf{Z})\right]=1 \tag{33}$$

The constraint condition Eq. (33) implies that the subspace of solutions to Eq. (26) must be one-dimensional. In this case the vector of wave amplitudes **A** is arbitrary to the extent that a scalar multiple of it is also a solution. Then the following constraint conditions are imposed,

$$A_{1,i}=1,\quad \begin{cases} A_{2,i}(m,\phi,\theta,\psi,\nu,\gamma)>0 \\ A_{3,i}(m,\phi,\theta,\psi,\nu,\gamma)>0, \quad i=1,2,3,4 \\ A_{4,i}(m,\phi,\theta,\psi,\nu,\gamma)>0 \end{cases} \tag{34}$$

$$\left(\frac{\partial \varpi_i}{\partial m}\right)_{\phi,\theta,\psi,\nu,\gamma}>0,\quad i=1,2,3,4 \tag{35}$$

The constraint condition Eq. (34) implies that the four nodes on the unit cell vibrate along the same direction. In molecular physics, condition Eq. (34) is called the restriction of the lattice spectrum to the acoustical branch [17]. Obviously, if the constraint condition Eq. (33) is not imposed, the constraint condition Eq. (34) is meaningless.

From Eq. (28) we obtain both the phase velocity and group velocity of the discretized media,

$$c_d=\frac{c}{2\pi}\frac{\varpi}{m},\quad c_{g,d}=\frac{\partial\omega}{\partial\kappa}=\frac{c}{2\pi}\frac{\partial\varpi}{\partial m} \tag{36}$$

Therefore, the constraint condition Eq. (35) is equivalent to

$$c_{g,d}>0 \tag{37}$$

It can be proven that for general periodic motion in lossless or low loss media the energy propagates with the group velocity [2]; therefore, the constraint condition Eq. (37) imposes that the energy propagates into the wave direction.

From this point, for each dispersion equation only the acoustical branch will be considered. This one represents the physically admissible solution for mechanical wave propagation.

It must be recall that the group velocity of the continuum will be equal to the phase velocity because the waves propagate non-dispersively. Nevertheless, for the dispersive discretized media the group velocity will be different from the phase velocity; therefore, the velocity of energy transport will be different from the phase velocity. As a consequence, when we consider the numerical dispersion associated with the finite element spatial discretization, not only the effect over the phase velocity must be analyzed but also the effect over the group velocity or velocity of energy transport.

2.3 Indicators of dispersion

By considering Eq. (36), the indicators of the dispersion associated with spatial discretization that is introduced by the finite element model are defined as

$$e_d=\frac{c_d}{c}=\frac{\varpi}{2m\pi},\quad e_d=e_d(m,\phi,\theta,\psi,\nu,\gamma) \tag{38}$$

$$e_{g,d} = \frac{c_{g,d}}{c} = \frac{1}{2\pi}\frac{\partial \varpi}{\partial m}, \quad e_{g,d} = e_{g,d}(m,\phi,\theta,\psi,\nu,\gamma) \tag{39}$$

These indicators consider the effect of the spatial discretization over the wave velocity and the velocity of energy transport, respectively. The indicators of spatial dispersion Eq. (38) and Eq. (39) are computed versus the dimensionless wave number both for longitudinal and transverse waves. Specifically, three test problems are analyzed in this paper, Figure 3.

For the Test A, the wave normal has direction parallel to two faces of the brick, and the polarization vector has direction either parallel to or perpendicular to those faces. Depending on the selected faces it can be distinguish three different cases:

$$\begin{aligned} &TEST \quad A-XY: \quad \phi = 0^{\circ}, \quad \theta = 0^{\circ}; \quad 0 \le \psi \le 90^{\circ}. \\ &TEST \quad A-XZ: \quad \phi = 0^{\circ}, \quad \theta = 90^{\circ}; \quad 0 \le \psi \le 90^{\circ}. \\ &TEST \quad A-YZ: \quad \phi = 90^{\circ}, \quad \theta = 90^{\circ}; \quad 0 \le \psi \le 90^{\circ}. \end{aligned} \tag{40}$$

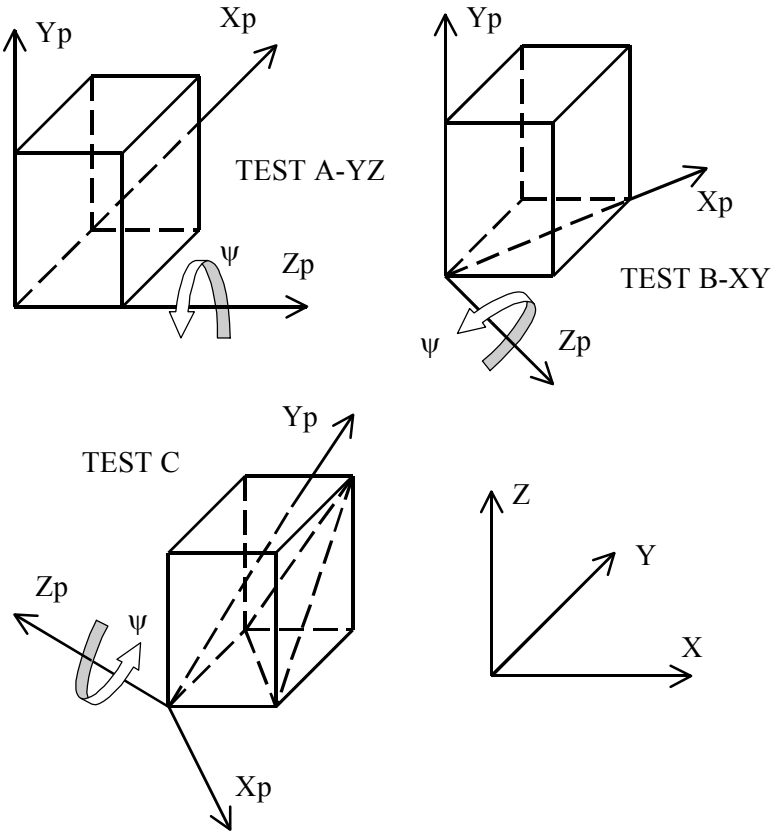

Figure 3: Test problems to evaluate the numerical dispersion.

For the Test B, the wave normal has direction parallel to a plane that diagonally intesects two opposite faces of the brick, and the polarization vector has direction either parallel to or perpendicular to that plane. Depending on the selected faces it can be distinguish three different cases:

$$
\begin{aligned}
&TEST \quad B-XY: \quad tg\phi = \frac{1}{\gamma^2}, \quad \theta = 90^{\circ}; \quad 0 \le \psi \le 90^{\circ}. \\
&TEST \quad B-XZ: \quad \phi = 90^{\circ}, \quad tg\theta = \frac{1}{\gamma}; \quad 0 \le \psi \le 90^{\circ}. \\
&TEST \quad B-YZ: \quad \phi = 0^{\circ}, \quad tg\theta = \gamma; \quad 0 \le \psi \le 90^{\circ}.
\end{aligned} \tag{41}
$$

For the Test C, the wave normal has direction parallel to a plane that diagonally intesects three faces of the brick, and the polarization vector has direction either parallel to or perpendicular to that plane,

$$
TEST \quad C: \quad tg\phi = -\frac{1}{\gamma^2}, \quad tg\theta = \sqrt{\gamma^2 + \frac{1}{\gamma^2}}; \quad 0 \le \psi < 180^{\circ}. \tag{42}
$$

For the Test C, a particular case of Eq. (38) is plotted in Figure 4. Three values of the angle of wave propagation are considered in order to represent the anisotropy induced by the spatial discretization. The dispersion associated with spatial discretization is clearly displayed as the dimensionless wave number increases.

It must be remarked that for the Test A and $\gamma = 1$, the values of Eq. (38) and Eq. (39) obtained both for longitudinal waves $\mathbf{n} = \hat{\mathbf{a}} = \mathbf{i}_p$ and transverse waves $\hat{\mathbf{a}} = \mathbf{j}_p$ are coincident with the ones obtained for the eight-node square element [4].

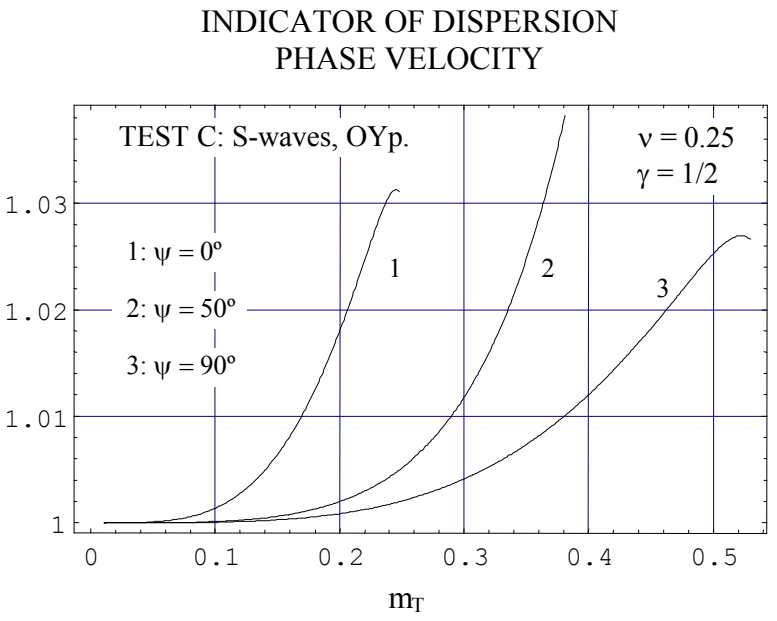

Figure 4: Test C. Indicator of spatial dispersion associated to the phase velocity versus dimensionless wave number for three values of the angle of wave propagation.

2.4 Higher order elastic energy at the unit cell

By considering the decomposition Eq. (18), in this paper we explore the relationship between the higher order elastic energy at the unit cell and the discretization error introduced by the finite element method. Assuming the harmonic waves Eq. (22), we obtain the higher order energy at the unit cell as the sum of the component associated with the corner node *A*,

$$
U_h^A = \rho c^2 (2b) F_h^A (m, \phi, \theta, \psi, \nu, \gamma, \tau) \tag{43}
$$

and the component associated with the mid-side nodes *B*, *C* and *D*,

$$U_h^M = \rho c^2 (2b) F_h^M (m,\phi,\theta,\psi,\nu,\gamma,\tau) \tag{44}$$

where: $\tau = t/T$, dimensionless time.

The period-averaged values,

$$\overline{F}_h^A (m,\phi,\theta,\psi,\nu,\gamma) = \int_0^1 F_h^A (m,\phi,\theta,\psi,\nu,\gamma,\tau) d\tau \tag{45}$$

$$\overline{F}_h^M (m,\phi,\theta,\psi,\nu,\gamma) = \int_0^1 F_h^M (m,\phi,\theta,\psi,\nu,\gamma,\tau) d\tau \tag{46}$$

are defined as the specific higher order corner energy and the specific higher order mid-side energy, respectively. The sum of these two components is the specific higher order energy at the unit cell.

The specific higher order corner and mid-side energies are computed versus the dimensionless wave number both for longitudinal and transverse waves. For the Test C, a particular case is plotted in Figures 5 and 6.

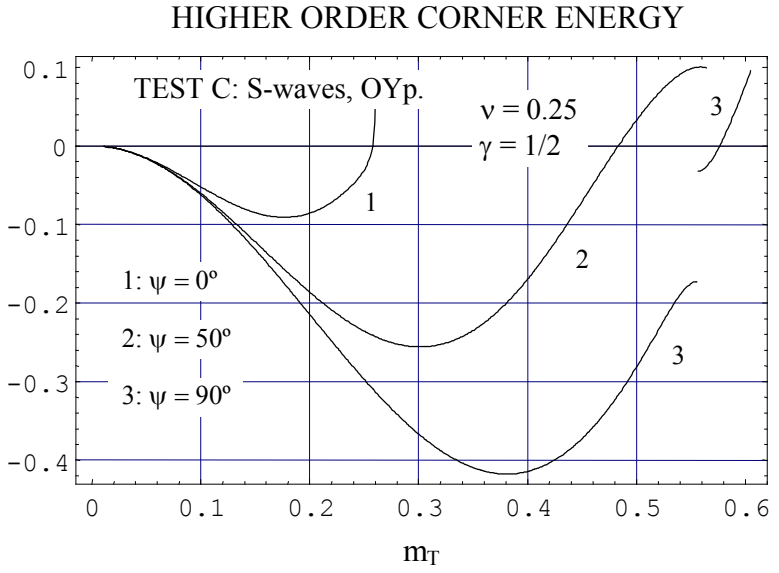

Figure 5: Test C. Specific higher order corner energy versus the dimensionless wave number.

We focus on the specific higher order corner energy. It is observed that the computed value decreases from zero as the dimensionless wave number increases until it reaches a minimum, then increases and eventually becomes positive. The sign-reversal value depends on the three Euler angles, the Poisson´s ratio and the aspect ratio parameter,

$$m_{L0}(\phi,\theta,\psi,\nu,\gamma), \quad m_{TY0}(\phi,\theta,\psi,\nu,\gamma), \quad m_{TZ0}(\phi,\theta,\psi,\nu,\gamma) \tag{47}$$

The first derivative of the specific higher order corner energy with respect to the dimensionless wave number is also computed. For the Tests C, a particular case is plotted in Figure 7. It is observed that the computed value decreases from zero as the dimensionless wave number increases until it reaches a minimum, then increases and eventually becomes positive. Obviously, the second derivative changes from negative to positive when the first

derivative reaches its local minimum. The sign-reversal value depends on the three Euler angles, the Poisson´s ratio and the aspect ratio parameter,

$$m_{L1}(\phi,\theta,\psi,\nu,\gamma), \quad m_{TY1}(\phi,\theta,\psi,\nu,\gamma), \quad m_{TZ1}(\phi,\theta,\psi,\nu,\gamma) \tag{48}$$

$$m_{L2}(\phi,\theta,\psi,\nu,\gamma), \quad m_{TY2}(\phi,\theta,\psi,\nu,\gamma), \quad m_{TZ2}(\phi,\theta,\psi,\nu,\gamma) \tag{49}$$

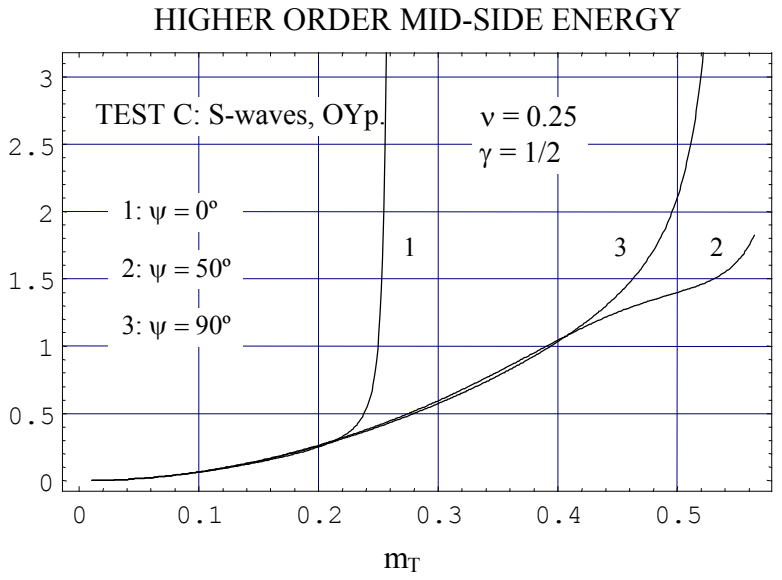

Figure 6: Test C. Specific higher order mid-side energy versus the dimensionless wave number.

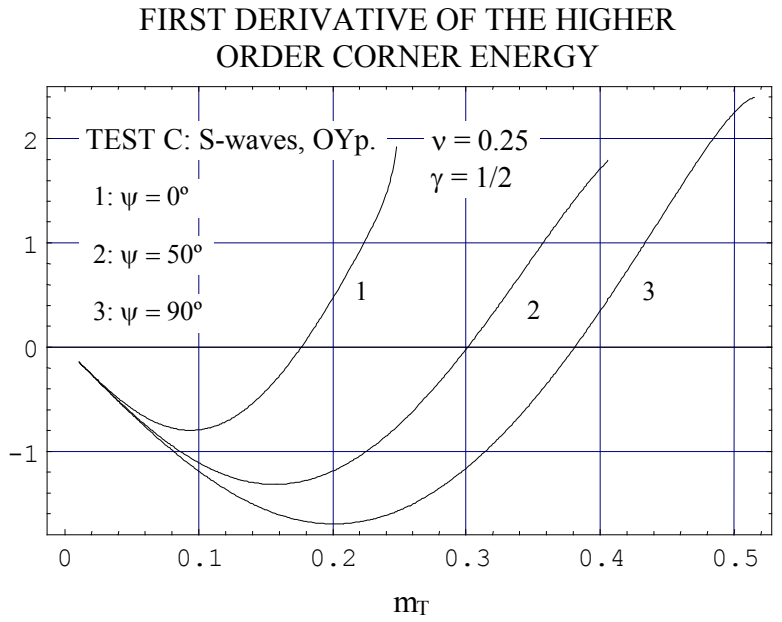

Figure 7: Test C. First derivative of the specific higher order corner energy versus the dimensionless wave number.

By also considering the behavior of the specific higher order mid-side energy, we can conclude that the components of the specific higher order energy at the unit cell satisfy the inequalities,

$$\overline{F}_h^A < 0, \quad \overline{F}_h^M > 0 \quad if \quad 0 < m < m_0 \tag{50}$$

$$\frac{\partial}{\partial m}\overline{F}_h^A < 0, \quad \frac{\partial}{\partial m}\overline{F}_h^M > 0 \quad if \quad 0 < m < m_1 \tag{51}$$

$$\frac{\partial^2}{\partial m^2}\overline{F}_h^A < 0, \quad \frac{\partial^2}{\partial m^2}\overline{F}_h^M > 0 \quad if \quad 0 < m < m_2 \tag{52}$$

where m_0, m_1 and m_2 are the values defined in Eq. (47)-(49).

Obviously, the specific higher order energy is always positive; nevertheless, as the discretization error decreases with the dimensionless wave number, it vanishes as a cancellation of two components, the positive mid-side energy and the negative corner energy. This behavior, which is called the cancellation property of the higher order energy at the unit cell, already has been observed by the author for the eight-node quadrilateral and the six-node triangle [4, 5]. Therefore, as the discretization error decreases, the higher order energy components tend to be equal but opposite in sign. By considering this evolution to the symmetry and the inequalities Eq. (50)-(52) we can conclude that the dimensionless wave numbers Eq. (47)-(49) determine behavioral ranges for the specific higher order energy. By considering this behavior, in this paper we propose to define Eq. (48) as the first reference wave number, and Eq. (49) as the second reference wave number. Both reference wave numbers basically depend on the three Euler angles and the aspect ratio parameter, and they exhibit a weak dependence respect to the Poisson´s ratio.

For a brick with cubic geometry, and for the Test A, in Tables 1 and 2 some computed values of the first and the second reference wave number are presented.

TEST A	$\gamma = 1$	$\nu = 0.45$	$\nu = 0.33$	$\nu = 0.25$	$\nu = 0.05$
$\psi = 0º$	P, OXp	0.3411	0.3411	0.3411	0.3411
	S, OYp	0.3411	0.3411	0.3411	0.3411
	S, OZp	0.3411	0.3411	0.3411	0.3411
$\psi = 25º$	P, OXp	0.3669	0.3738	0.3738	0.3728
	S, OYp	0.3689	0.3629	0.3629	0.3639
	S, OZp	0.3679	0.3679	0.3679	0.3679
$\psi = 37.5º$	P, OXp	0.3877	0.3897	0.3887	0.3877
	S, OYp	0.4154	0.3916	0.3887	0.3867
	S, OZp	0.3857	0.3857	0.3857	0.3857
$\psi = 45º$	P, OXp	0.3976	0.3906	0.3897	0.3887
	S, OYp	0.4273	0.3996	0.3966	0.3926
	S, OZp	0.3897	0.3897	0.3897	0.3897

Table 1: Test A. Dimensionless wave number for which the sign of the first derivative of the specific higher order corner energy changes from negative to positive.

For non-cubic brick, and for each of the test problems, some computed values of the first and the second reference wave number are plotted in Figures 8-10. It must be remarked that the strong numerical anisotropy induced by the non-cubic brick results in broad variations of

both reference wave numbers versus the angle of wave propagation. Clearly, the numerical anisotropy increases as the aspect ratio parameter decreases.

TEST A	$\gamma = 1$	$\nu = 0.45$	$\nu = 0.33$	$\nu = 0.25$	$\nu = 0.05$
$\psi = 0^o$	P, OXp	0.1813	0.1813	0.1813	0.1813
	S, OYp	0.1813	0.1813	0.1813	0.1813
	S, OZp	0.1813	0.1813	0.1813	0.1813
$\psi = 25^o$	P, OXp	0.1951	0.1951	0.1941	0.1941
	S, OYp	0.1931	0.1912	0.1922	0.1922
	S, OZp	0.1931	0.1931	0.1931	0.1931
$\psi = 37.5^o$	P, OXp	0.2100	0.2060	0.2050	0.2040
	S, OYp	0.2050	0.2001	0.2001	0.2001
	S, OZp	0.2021	0.2021	0.2021	0.2021
$\psi = 45^o$	P, OXp	0.2129	0.2090	0.2080	0.2060
	S, OYp	0.2080	0.2021	0.2021	0.2021
	S, OZp	0.2030	0.2030	0.2030	0.2030

Table 2: Test A. Dimensionless wave number for which the sign of the second derivative of the specific higher order corner energy changes from negative to positive.

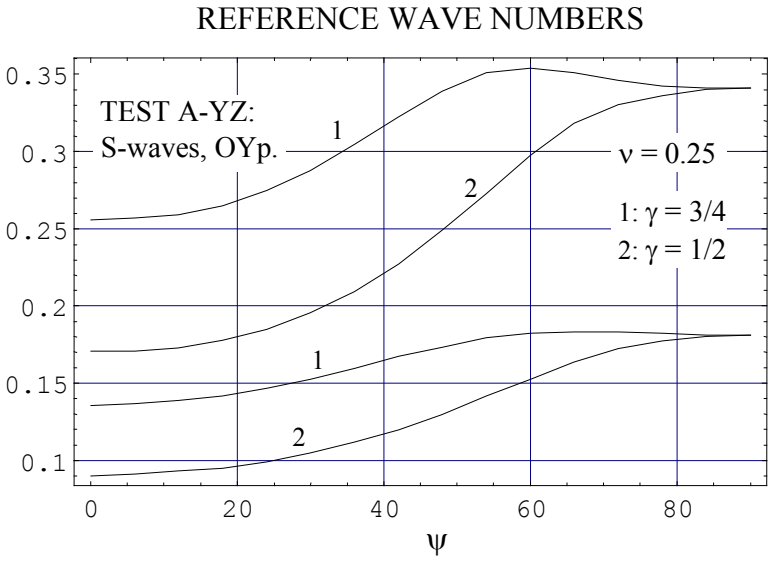

Figure 8: Test A-YZ. Reference wave numbers versus the angle of wave propagation.

Both reference wave numbers decrease as the angle of wave propagation exhibits a higher numerical dispersion, as it is observed for the Test C in Figures 4, 5 and 7. By considering this property, we investigate the use of one of the reference wave numbers as optimum cutoff wave number to properly capture the harmonic wave.

For the Test C, in Figures 11 and 12 we compute the maximum of Eq. (38) and the maximum of Eq. (39), respectively, for dimensionless wave number up to reach the first reference value. In this case, we consider that the harmonic wave is only properly captured from the wave velocity standpoint. In Figure 13 we compute the maximum of Eq. (39) for dimensionless wave number up to reach the second reference value. In this case, we consider

that the harmonic wave is properly captured also from the velocity of energy transport standpoint. Similar results have been obtained for the Test A and the Test B.

We can conclude that, depending on the desired precision, the reference wave numbers could be used as optimum cutoff wave numbers tuned to taking into account the effect of the numerical anisotropy induced by the spatial discretization. The tuning effect can be clearly observed for the Test C by considering Figures 4, 5 and 7.

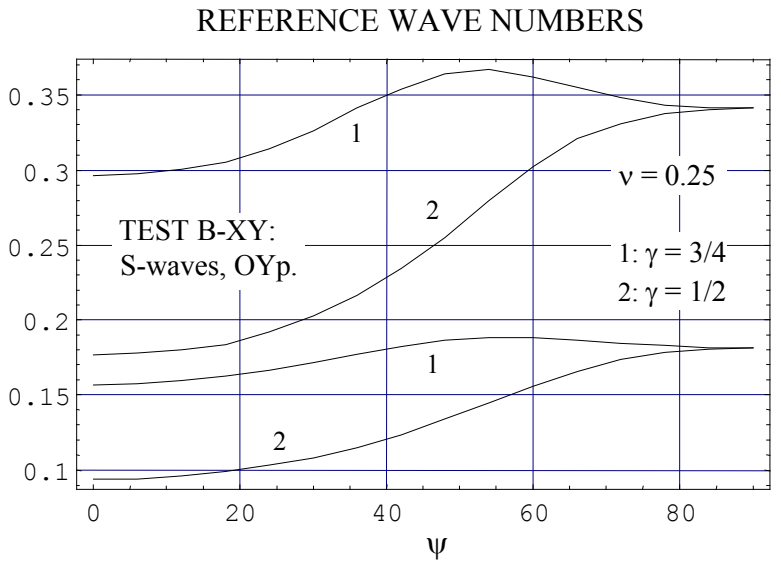

Figure 9: Test B-XY. Reference wave numbers versus the angle of wave propagation.

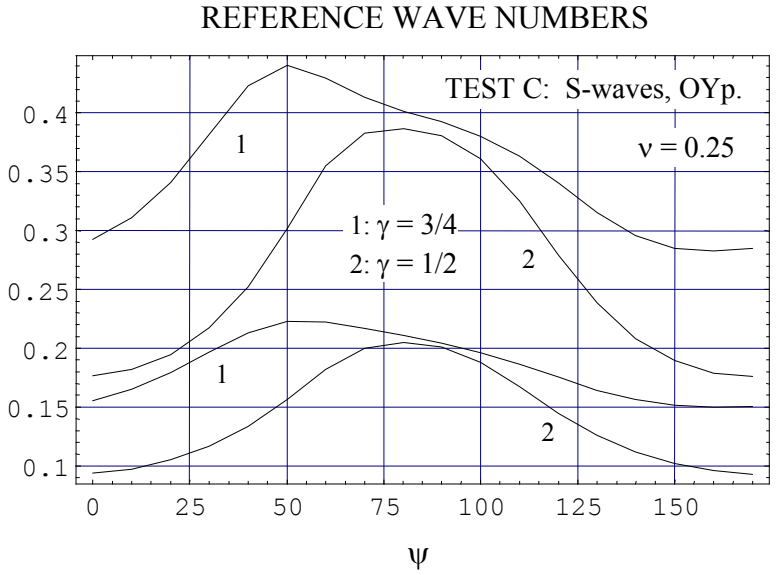

Figure 10: Test C. Reference wave numbers versus the angle of wave propagation.

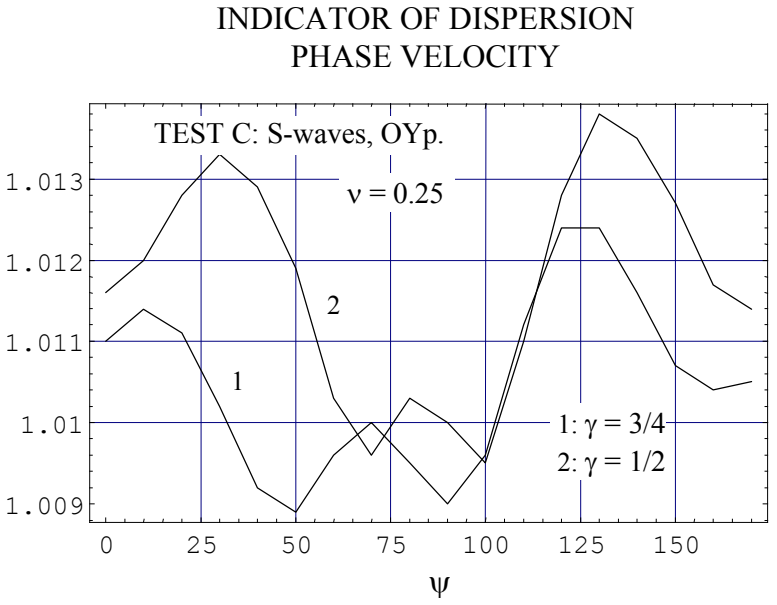

Figure 11: Test C. Maximum of the indicator of spatial dispersion associated to the phase velocity for dimensionless wave number up to reach the first reference value versus the angle of wave propagation.

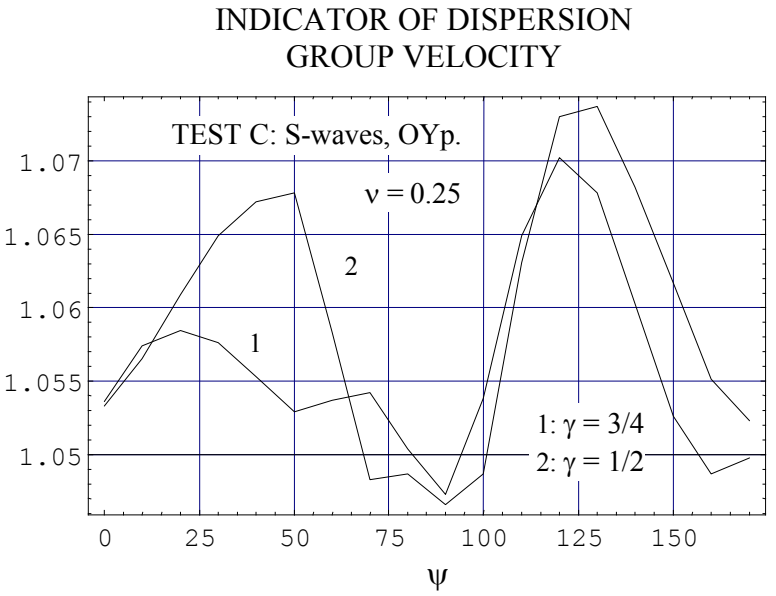

Figure 12: Test C. Maximum of the indicator of spatial dispersion associated to the group velocity for dimensionless wave number up to reach the first reference value versus the angle of wave propagation.

The mean values of the first reference wave number and the ones of the second reference wave number are computed in Tables 3 and 4, respectively, for each of the test problems. By considering the minimum mean values computed for the tests A and B, which are obtained for the cases Test A-YZ and Test B-XY, and the mean values computed for the Test C, we propose to select the values,

$$\gamma = 1: \quad m_1 = 0.38, \quad m_2 = 0.2 \tag{53}$$

$$\gamma = 0.75: \quad m_1 = 0.33, \quad m_2 = 0.17 \tag{54}$$

$$\gamma = 0.5: \quad m_1 = 0.25, \quad m_2 = 0.13 \tag{55}$$

as the first and the second standard reference wave number, respectively. Both standard reference wave numbers decrease as the distortion of the regular mesh increases.

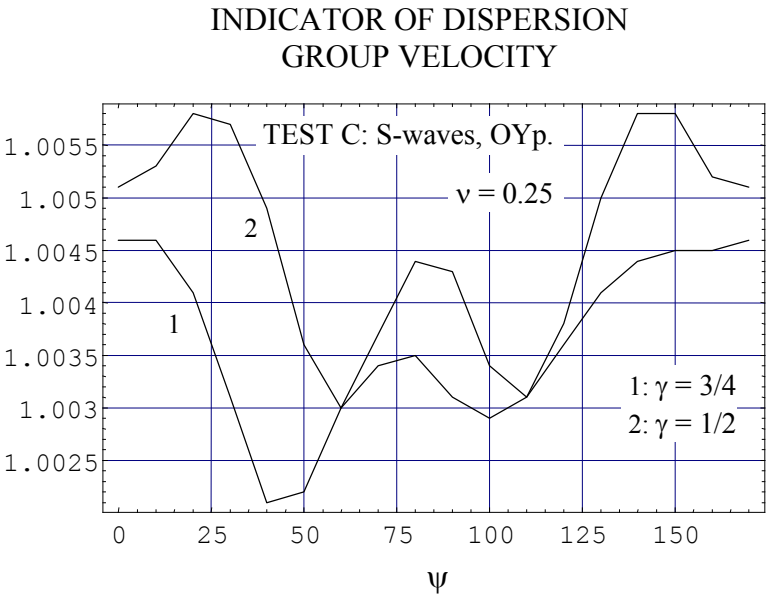

Figure 13: Test C. Maximum of the indicator of spatial dispersion associated to the group velocity for dimensionless wave number up to reach the second reference value versus the angle of wave propagation.

	ν = 0.25	γ = 1	γ = 3/4	γ = 1/2
TEST A				
XY	S, OYp	0.3723	0.3559	0.3293
	S, OZp	0.3711	0.3558	0.3262
XZ	S, OYp	0.3723	0.4159	0.4993
	S, OZp	0.3711	0.4171	0.4989
YZ	S, OYp	0.3723	0.3120	0.2497
	S, OZp	0.3711	0.3127	0.2494
TEST B				
XY	S, OYp	0.3842	0.3348	0.2544
	S, OZp	0.3875	0.3333	0.2531
XZ	S, OYp	0.3842	0.3395	0.2630
	S, OZp	0.3875	0.3372	0.2591
YZ	S, OYp	0.3842	0.3901	0.3514
	S, OZp	0.3875	0.3917	0.3481
TEST C				
	S, OYp	0.3914	0.3541	0.2658
	S, OZp	0.3916	0.3507	0.2615

Table 3: Mean values of the dimensionless wave number for which the sign of the first derivative of the specific higher order corner energy changes from negative to positive.

The use of one of the standard reference wave numbers as optimum cutoff wave number to properly capture an arbitrary interference field composed of both longitudinal and transverse harmonic waves is also investigated. To approach this question, the computation of natural modes when a solid is discretized by a regular mesh will be analyzed.

		$\nu = 0.25$	$\gamma = 1$	$\gamma = 3/4$	$\gamma = 1/2$
TEST A					
XY	S, OYp	0.1939	0.1875	0.1750	
	S, OZp	0.1949	0.1883	0.1755	
XZ	S, OYp	0.1939	0.2186	0.2633	
	S, OZp	0.1949	0.2199	0.2645	
YZ	S, OYp	0.1939	0.1641	0.1315	
	S, OZp	0.1949	0.1648	0.1323	
TEST B					
XY	S, OYp	0.1998	0.1758	0.1341	
	S, OZp	0.1998	0.1758	0.1345	
XZ	S, OYp	0.1998	0.1773	0.1385	
	S, OZp	0.1998	0.1772	0.1386	
YZ	S, OYp	0.1998	0.2042	0.1866	
	S, OZp	0.1998	0.2042	0.1865	
TEST C					
	S, OYp	0.2025	0.1843	0.1401	
	S, OZp	0.2021	0.1838	0.1400	

Table 4: Mean values of the dimensionless wave number for which the sign of the second derivative of the specific higher order corner energy changes from negative to positive.

3 MODAL ANALYSIS

In order to properly capture a natural mode, a discretized solid must properly capture both the longitudinal and transverse waves with frequency equal to the associated natural frequency. From the inequality $m_L < m_T$ we deduce that if the solid discretized by a regular mesh properly captures the transverse waves also properly captures the longitudinal waves; obviously, the inverse is not true.

From Eq. (7) and Eq. (28), given the dimensionless wave number based on the transverse wave, we obtain the associated frequency at the continuum, for the solid discretized by a regular mesh,

$$f_T = \frac{c_T}{2b} m_T \tag{56}$$

From Eq. (56) and Eq. (53)-(55) we obtain the first and the second reference frequency. Both reference frequencies depend on the aspect ratio parameter.

Two test problems will be analyzed: the clamped block and the cantilever beam [18], which are discretized by the regular meshes represented in Figure 14. The clamped block is a relatively bulk solid which is discretized by a moderately distorted mesh. The cantilever beam is a slender structural element which is discretized by a highly distorted mesh. For the clamped block: Young´s modulus, $E = 68.95 \times 10^9$ Pa; Poisson´s ratio, $\nu = 0.3$; mass density per unit volume of the material, $\rho = 2560$ kg/m^3; aspect ratio parameter, $\gamma = 3/4$. For the

cantilever beam: Young´s modulus, $E = 2.068 \times 10^{11}$ Pa; Poisson´s ratio, $\nu = 0.3$; mass density per unit volume of the material, $\rho = 8058$ kg/m^3; aspect ratio parameter, $\gamma = 1/2$.

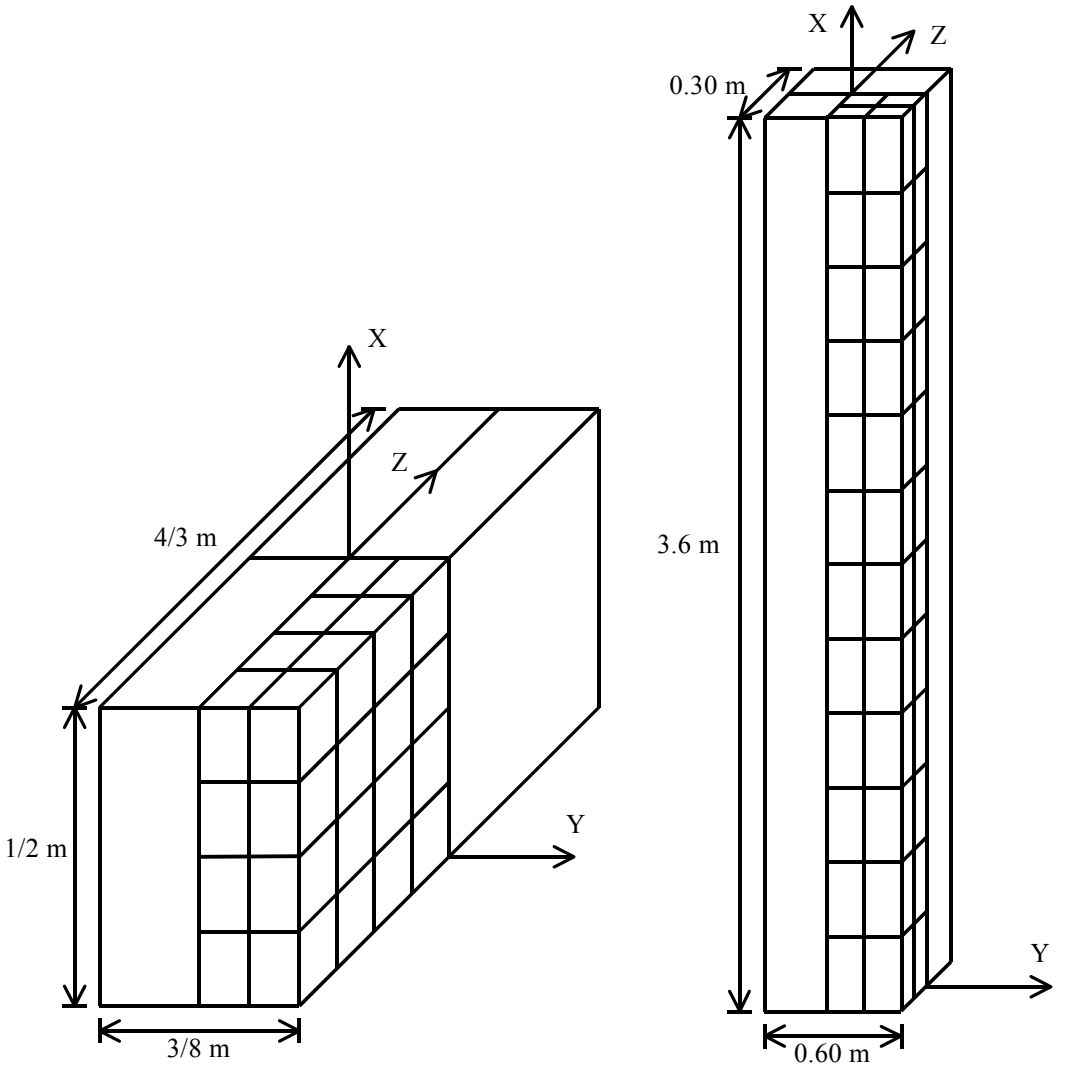

Figure 14: Clamped block and cantilever beam.

The reference frequencies for the clamped block and the cantilever beam are, respectively,

$$f_{T1} = 8496.98 \quad Hz, \quad f_{T2} = 4377.23 \quad Hz \tag{57}$$

and

$$f_{T1} = 5236.29 \quad Hz \quad f_{T2} = 2722.87 \quad Hz \tag{58}$$

An estimation of the error for the natural frequencies and modes obtained with the discretized solid is presented. In each case the reference model is obtained by dividing each element of the actual mesh into eight elements. The natural frequencies and the modal displacements obtained with the actual model and the ones obtained with the reference model are compared by the frequency error and the correlated coefficient for modal vector [19], respectively,

$$FE = \frac{\omega - \omega_{ref}}{\omega_{ref}} x100 \tag{59}$$

$$CCFMV = \frac{\left|\boldsymbol{\varphi}^t \cdot \boldsymbol{\varphi}_{ref}\right|}{(\boldsymbol{\varphi}^t \cdot \boldsymbol{\varphi})^{1/2} (\boldsymbol{\varphi}_{ref}^t \cdot \boldsymbol{\varphi}_{ref})^{1/2}} \tag{60}$$

The vectors in Eq. (60) are obtained by computing each modal displacement at the nodes of the reference mesh. A value of *CCFMV* close to 1 suggests that the two vectors are well correlated, and a value close to 0 indicates uncorrelated vectors. A poor correlation between the results obtained with the actual model and the ones obtained with the reference model is indicated by frequency error greater than 5, and by *CCFMV* less than 0.90 [20].

For the test problems, in Tables 5-8 we present the evolution of Eq. (59) and Eq. (60) versus the natural frequency computed by the actual model.

MODE	FR (Hz)	FE	CCFMV	MODE	FR (Hz)	FE	CCFMV
SS				SA			
1	2199.821	0.179	1.000	1	971.640	0.534	1.000
2	2727.118	0.185	1.000	2	1613.714	0.274	1.000
3	3042.302	0.133	1.000	3	2950.334	0.440	1.000
4	4056.529	0.430	1.000	4	3344.607	0.374	1.000
5	5346.486	0.817	0.999	5	3763.871	0.425	1.000
6	5590.840	0.238	1.000	6	4901.894	0.575	1.000
7	6065.390	0.790	0.996	7	5164.174	0.725	1.000
8	6346.069	0.361	0.984	8	5483.621	0.544	0.999
9	6426.352	0.573	0.975	9	5613.046	0.618	0.999
10	6645.206	0.744	0.971	10	5963.634	0.511	0.999
11	6746.201	0.410	0.967	11	6288.133	1.725	0.997
12	6817.067	0.821	0.956	12	6863.180	1.421	0.997
13	7172.877	0.741	0.983	13	7036.543	1.216	0.993
14	7297.092	1.656	0.978	14	7211.806	1.071	0.540
15	7433.359	1.183	0.996	15	7275.739	1.850	0.558
16	7797.719	1.442	0.990	16	7585.119	1.276	0.988
17	8070.746	1.607	0.981	17	7867.853	1.356	0.989
18	8169.500	1.548	0.971	18	8201.079	1.961	0.981
19	8424.037	1.451	0.941	19	8329.689	1.378	0.987
20	8557.213	1.191	0.976	20	8827.818	3.605	0.038
21	8671.875	1.517	0.896	21	8987.235	3.102	0.183
22	8850.724	2.430	0.190	22	9085.131	2.468	0.097
23	8974.079	2.743	0.145	23	9259.918	2.966	0.007
24	9170.113	2.203	0.134	24	9617.571	3.690	0.396
25	9371.654	3.674	0.258	25	9827.690	4.762	0.031
26	9458.243	3.038	0.414	26	10057.981	5.405	0.082
27	9538.228	2.566	0.179	27	10269.557	5.395	0.415
28	9675.288	3.585	0.565	28	10296.553	4.117	0.096
29	9842.971	2.247	0.851	29	10403.791	4.255	0.314
30	9891.466	2.295	0.861	30	10515.302	3.554	0.588

Table 5: Clamped block. Frequency error and correlated coefficient for modal vector versus the computed natural frequency. Modes SS and SA.

For the clamped block is observed that whenever the computed natural frequency is less than the second reference frequency the results obtained with the actual model and the ones obtained with the reference model exhibit a high correlation. The results in the range between the second reference frequency and the first one are generally well correlated; nevertheless, if the first reference frequency is gone through the results clearly exhibit a poor correlation.

For the cantilever beam is observed that whenever the computed natural frequency is less than the second reference frequency the results obtained with the actual model and the ones obtained with the reference model exhibit a high correlation or, alternatively, a good correlation; nevertheless, in the range between the second reference frequency and the first one a non-negligible number of modes exhibit a poor correlation.

MODE	FR (Hz)	FE	CCFMV	MODE	FR (Hz)	FE	CCFMV
AS				AA			
1	1425.965	0.267	1.000	1	1131.355	0.418	1.000
2	2742.309	0.124	1.000	2	2399.369	0.275	1.000
3	3298.543	0.206	1.000	3	3143.737	0.402	1.000
4	4115.889	0.138	1.000	4	4145.977	0.425	1.000
5	4670.003	0.594	1.000	5	4551.929	0.489	1.000
6	5347.425	0.600	0.999	6	5097.987	0.618	0.993
7	6138.249	0.698	0.981	7	5193.445	0.593	0.996
8	6201.578	0.568	0.984	8	5589.388	0.491	1.000
9	6447.421	0.321	0.999	9	6061.990	0.964	0.998
10	6702.224	0.370	0.991	10	6420.540	1.052	0.997
11	6759.073	0.611	0.991	11	6489.071	0.614	0.998
12	6973.841	0.962	0.964	12	6907.589	1.205	0.966
13	7132.266	1.647	0.953	13	7003.408	0.687	0.966
14	7339.887	1.116	0.966	14	7453.756	2.415	0.957
15	7696.521	1.236	0.980	15	7788.464	2.590	0.956
16	7962.018	2.898	0.959	16	7959.445	1.579	0.942
17	8065.381	1.591	0.965	17	8068.548	1.748	0.948
18	8125.485	0.861	0.967	18	8597.211	2.834	0.359
19	8411.192	1.882	0.802	19	8650.454	1.667	0.281
20	8461.104	1.145	0.813	20	8824.951	0.859	0.984
21	8781.663	1.964	0.992	21	9012.522	1.964	0.968
22	8852.156	1.780	0.989	22	9158.781	2.621	0.970
23	9167.227	1.706	0.968	23	9431.149	1.110	0.982
24	9250.645	1.851	0.970	24	9624.671	1.708	0.386
25	9427.560	1.937	0.950	25	9947.605	4.385	0.240
26	9522.444	2.017	0.547	26	10081.541	3.585	0.361
27	9599.327	2.587	0.555	27	10318.279	4.558	0.588
28	9772.311	2.631	0.695	28	10399.856	3.357	0.513
29	9890.698	2.122	0.409	29	10720.404	4.805	0.862
30	10066.772	3.013	0.253	30	10908.133	4.860	0.043

Table 6: Clamped block. Frequency error and correlated coefficient for modal vector versus the computed natural frequency. Modes AS and AA.

4 CONCLUSIONS

This paper studies the propagation of plane harmonic waves in unbounded media discretized by the standard twenty-node hexahedral finite element. The element stiffness matrix is split into basic and higher order components which are obtained from mean and deviatoric strain fields, respectively. This decomposition is applied to the elastic energy. The research is focused on the properties of the higher order elastic energy versus the wave number. Based on the properties of the higher order energy, two values of the wave number are selected as reference values. The noteworthy conclusions of this paper are:

MODE	FR (Hz)	FE	CCFMV	MODE	FR (Hz)	FE	CCFMV
SS				SA			
1	353.417	0.082	1.000	1	37.380	0.218	1.000
2	1057.604	0.087	1.000	2	209.804	0.225	1.000
3	1752.870	0.106	1.000	3	516.261	0.249	1.000
4	2428.493	0.155	1.000	4	881.088	0.312	1.000
5	3058.068	0.256	1.000	5	1279.072	0.443	1.000
6	3569.675	0.425	0.999	6	1693.375	0.662	1.000
7	3701.198	0.336	1.000	7	2114.270	0.978	1.000
8	3899.181	0.686	0.999	8	2514.574	1.216	0.998
9	4129.715	0.984	0.990	9	2740.195	0.360	0.994
10	4166.233	0.160	0.992	10	2866.200	1.003	0.991
11	4175.800	0.136	0.998	11	3120.875	1.247	0.985
12	4264.840	0.214	0.988	12	3263.999	1.205	0.983
13	4286.941	0.456	0.939	13	3595.522	2.209	0.960
14	4385.815	1.182	0.891	14	3713.496	1.487	0.951
15	4405.419	0.414	0.937	15	4103.630	3.509	0.919
16	4624.747	2.380	0.985	16	4191.904	1.596	0.899
17	4837.400	2.416	0.774	17	4634.283	5.162	0.935
18	4955.171	2.304	0.761	18	4668.742	1.214	0.965
19	5259.268	5.054	0.886	19	5130.796	5.919	0.702
20	5371.512	1.860	0.146	20	5303.737	3.959	0.468

Table 7: Cantilever beam. Frequency error and correlated coefficient for modal vector versus the computed natural frequency. Modes SS and SA.

- The numerical research reveals that the first reference wave number could be used as an optimum cutoff wave number to properly capture an harmonic wave from the wave velocity standpoint. For dimensionless wave number less than the second reference wave number the harmonic wave would be properly captured also from the velocity of energy transport standpoint.
- The strong numerical anisotropy induced by the non-cubic meshes results in broad variations of both reference wave numbers versus the direction of wave propagation; nevertheless, by considering the mean values, the first and the second standard reference wave number can be defined. These ones depend on the aspect ratio parameter. Given the standard reference wave numbers based on the transverse wave, the first and the second reference frequency are defined.
- The numerical research reveals that a finite element natural mode exhibits a high precision or, alternatively, a good precision whenever the natural frequency is less than

the second reference frequency; nevertheless, in the range between the second reference frequency and the first one, the precision of the natural modes is clearly depending on the problem. Generally, it could be regarded that, in the range between the second reference frequency and the first one, the finite element model has an intermediate precision.

The consideration of more complex waves and media is subject of research.

MODE	FR (Hz)	FE	CCFMV	MODE	FR (Hz)	FE	CCFMV
AS				AA			
1	19.041	0.239	1.000	1	164.960	0.217	1.000
2	115.702	0.283	1.000	2	496.209	0.230	1.000
3	310.034	0.372	1.000	3	831.344	0.266	1.000
4	574.523	0.532	1.000	4	1172.703	0.344	1.000
5	893.127	0.788	1.000	5	1522.456	0.491	1.000
6	1252.357	1.171	1.000	6	1882.767	0.740	1.000
7	1643.297	1.714	1.000	7	2255.951	1.128	1.000
8	2060.514	2.448	0.999	8	2644.537	1.700	0.999
9	2499.275	3.367	0.998	9	3051.184	2.495	0.998
10	2849.359	1.745	0.870	10	3478.099	3.545	0.997
11	2909.888	1.099	0.717	11	3924.298	4.820	0.992
12	2990.308	2.269	0.699	12	4366.385	5.878	0.950
13	3034.928	0.675	0.929	13	4579.422	2.468	0.976
14	3180.253	0.504	0.992	14	4708.509	0.975	0.755
15	3365.136	2.755	0.514	15	4733.350	0.914	0.616
16	3491.702	3.746	0.506	16	4778.153	1.256	0.558
17	3606.540	0.696	0.989	17	4856.998	1.590	0.508
18	3873.630	4.370	0.204	18	4955.099	2.154	0.423
19	4022.877	4.693	0.198	19	5086.594	2.591	0.320
20	4179.955	1.586	0.927	20	5231.727	3.745	0.118
21	4382.056	5.620	0.878	21	5400.464	4.503	0.062
22	4521.035	2.244	0.979				
23	4885.734	6.862	0.175				
24	5135.984	8.367	0.155				
25	5294.493	6.096	0.253				

Table 8: Cantilever beam. Frequency error and correlated coefficient for modal vector versus the computed natural frequency. Modes AS and AA.

REFERENCES

[1] H.L. Schreyer, Dispersion of semidiscretized and fully discretized systems. T. Belytschko, T.J.R. Hughes eds. *Computational methods for transient analysis*. Elsevier Science, 1983.

[2] J.D. Achenbach, *Wave propagation in elastic solids*. Elsevier, 1975.

[3] K.F. Graff, *Wave motion in elastic solids*. Dover Publications, 1991.

[4] F.J. Brito Castro, Cutoff wave numbers for energy-orthogonal eight-node quadrilateral plane-strain elements. *Computers and Structures*, **84**, 230-242, 2006.

[5] F.J. Brito Castro, Cutoff wave numbers for energy-orthogonal six-node triangular plane-strain elements. *Computers and Structures*, **87**, 395-406, 2009.

[6] O.C. Zienkiewicz, R.L. Taylor, *The finite element method, Vol. 1*. Butterworth-Heinemann, 2000.

[7] R.D. Cook, D.S. Malkus, M.E. Plesha, *Concepts and applications of finite element analysis*. John Wiley & Sons, 1989.

[8] C.A. Felippa, B. Haugen, C. Militello, From the individual element test to finite element templates: evolution of the Patch Test. *International Journal for Numerical Methods in Engineering*, **38**, 199-229, 1995.

[9] P.G. Bergan, M.K. Nygärd, Finite elements with increased freedom in choosing shape functions. *International Journal for Numerical Methods in Engineering*, **20**, 643-664, 1984.

[10] C.A. Felippa, A survey of parametrized variational principles and applications to computational mechanics. *Computer Methods in Applied Mechanics and Engineering*, **113**, 109-139, 1994.

[11] F.J. Brito Castro, A modal error indicator based on a work-cancellation property of energy-orthogonal quadrilateral and hexahedral finite elements. *International Journal for Computational Methods in Engineering Science and Mechanics*, **6**, 127-135, 2005.

[12] K.J. Bathe, *Finite element procedures*. Prentice Hall, 1996.

[13] A.A. Shabana, *Computational dynamics*. John Wiley & Sons, 1994.

[14] M. Okrouhlík, C. Höschl, A contribution to the study of dispersive properties of one-dimensional lagrangian and hermitian elements. *Computers and Structures*, **49**, 779-795, 1993.

[15] R.A. Horn, C.R. Johnson, *Matrix analysis*. Cambridge University Press, 1992.

[16] W.H. Press, S.A. Teukolsky, W.T. Vetterling, B.P. Flannery, *Numerical recipes in fortran*. Cambridge University Press, 1992.

[17] L. Brillouin, *Wave propagation in periodic structures*. McGraw-Hill, 1946.

[18] M. Petyt, *Introduction to finite element vibration analysis*. Cambridge University Press, 1990.

[19] Z-Q. Qu, *Model order reduction techniques: with applications in finite element analysis*. Springer, 2004.

[20] F.M. Hemez, *Theoretical and experimental correlation between finite element models and modal tests in the context of large flexible space structures*, Ph.D. Thesis. University of Colorado, 1993.